

Brushlets : Steerable Wavelet Packets

François G. Meyer
Ronald R. Coifman

Abstract. We address the problem of describing an image with a library of steerable wavelet packets. Inspired by the duality between local trigonometric bases and wavelet packets, we construct wavelet packets of two variables in the Fourier domain using local Fourier bases. Our wavelet packets, called brushlets, are complex valued functions with a phase. We show that the brushlets can resolve without any ambiguity many more orientations than standard wavelet packets. In theory our brushlets have infinite support. However we show that a careful design of the window of the local Fourier basis yields a brushlet with a very fast decay.

1. Introduction

Edges and textures in an image can exist at all possible locations, orientations, and scales. The ability to efficiently analyze and describe textured patterns is thus of fundamental importance for image analysis and image compression. The simplest model of a patch of periodic texture located at (x_0, y_0) is provided by a windowed complex exponential :

$$w(x - x_0, y - y_0)e^{i(\xi x + \eta y)} \quad (1.1)$$

where w is a function localized around the origin. Obviously, a local Fourier basis provides the most appropriate tool for the analysis of this patch of texture. In order to encode the entire image with local Fourier bases, one can divide the image in adjacent blocks of constant size, and then compute a Fourier expansion within each block. While this approach is easy to implement, it suffers from a number of drawbacks :

1. The size of the blocks should be adapted to the content inside the image : a large geometric feature should not belong to several small blocks, but should belong to a single large block.
2. The size of the blocks should be adapted to the frequencies of the complex exponential : short blocks for high frequency, large blocks for low frequencies.
3. The segmentation into blocks creates “blocking” artifacts when the transform is used for image coding.

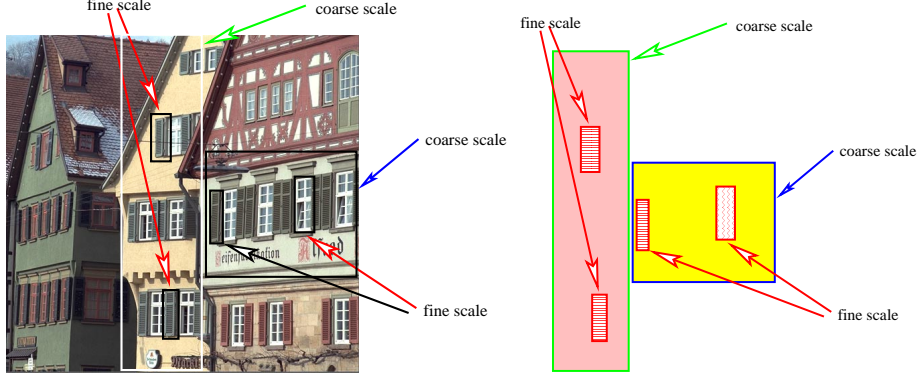


Figure 1. Small scale blocks that describe the shutters or the windows need to overlap on large scale blocks that describe the buildings. One cannot perform this type of analysis with local Fourier bases. As shown on the right one needs to have basis functions that lay over each others .

4. One cannot have block of different sizes superimposed onto each others. As shown in figure 1, one should be able to describe the background with a large scale window, and the small foreground objects with small scale windows.

These issues can be solved if we replace the Fourier analysis with a multiresolution analysis such as the wavelet transform [6]. Two dimensional wavelet bases that are used in practice are tensor products of one dimensional bases. Let φ be a scaling function, and let ψ be the corresponding wavelet, we define four wavelet functions as follows :

$$\psi_k(x, y) = \begin{cases} \varphi(x)\varphi(y) & \text{if } k = 0 \\ \varphi(x)\psi(y) & \text{if } k = 1 \\ \psi(x)\varphi(y) & \text{if } k = 2 \\ \psi(x)\psi(y) & \text{if } k = 3 \end{cases} \quad (1..2)$$

The associated filter banks $m_k(\xi, \eta)$, $k = 1, 2, 3$ can resolve 2.5 directions : horizontal, vertical and an undecided diagonal/anti-diagonal direction (see Figure 2). Replacing the octave band decomposition with a more general splitting of the Fourier domain allows us to resolve more orientations. Wavelet packets make it possible to adaptively construct an optimal tiling of the Fourier plane, and they have been used for image compression [10, 13]. However the tensor product of two real valued wavelet packets is always associated with four symmetric peaks in the frequency plane. The geometric interpretation of a large wavelet packet coefficient becomes then problematic : the intensity in the image is either oscillating as planar wave $e^{i(\omega_x x + y \omega_y y)}$, or it is oscillating with the conjugate frequency $e^{i(\omega_x x - y \omega_y y)}$. In order to remove the ghost in the conjugate

direction, one needs to use filters that are zero in the upper left and lower right quadrants, or in the upper right and lower left quadrants. For instance, we could have (see Figure 3) :

$$m_3(\xi, \eta) = 0 \quad \text{if } \xi > 0 \quad \text{and} \quad \eta < 0, \quad \text{or if } \xi < 0 \quad \text{and} \quad \eta > 0 \quad (1..3)$$

In order to construct such filters one could use two wavelets ψ_g and ψ_h that form an (approximate) Hilbert pair :

$$\psi_g(\xi) = \begin{cases} -i\psi_h(\xi), & \text{if } \xi > 0 \\ i\psi_h(\xi), & \text{if } \xi < 0 \end{cases} \quad (1..4)$$

with φ_h, φ_g being the corresponding scaling functions. Unfortunately, any tensor products of the form $\psi_h(x)\psi_g(y)$ will have its Fourier transform localized in only one quadrant. One way to solve this problem is to consider the tensor products of the wavelet ψ_h :

$$\begin{aligned} \psi_{h,1}(x, y) &= \varphi_h(x)\psi_h(y) \\ \psi_{h,2}(x, y) &= \psi_h(x)\varphi_h(y) \\ \psi_{h,2}(x, y) &= \psi_h(x)\psi_h(y) \end{aligned} \quad (1..5)$$

Similar tensor products $\psi_{g,k}$, $k = 1, 2, 3$ can be defined for the wavelet ψ_g . One can then compute sums and differences of the wavelets $\psi_{h,k}$ and $\psi_{g,k}$, as was suggested by Selesnick in [14] :

$$\begin{aligned} \psi_i(x, y) &= \psi_{h,i}(x, y) + \psi_{g,i}(x, y) \\ \psi_{i+3}(x, y) &= \psi_{h,i}(x, y) - \psi_{g,i}(x, y) \quad i = 0, 1, 2 \end{aligned} \quad (1..6)$$

The filters m_i associated to the functions ψ_i are shown in Figure 4. A discrete implementation is obtained by combining two wavelet transforms associated with ψ_h and ψ_g respectively. The sums and differences of the coefficients are

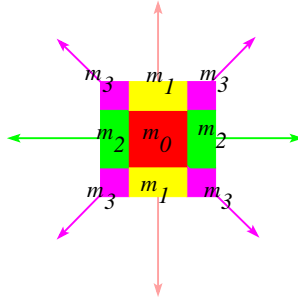


Figure 2. The wavelet filter banks m_1, m_2, m_3 can resolve 2.5 directions : horizontal, vertical and an undecided diagonal/anti-diagonal direction .

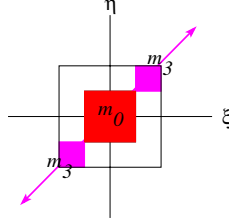


Figure 3. The filter m_3 can resolve the diagonal direction .

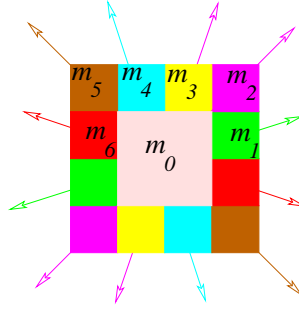


Figure 4. A 2 times redundant wavelet transform can resolve 6 directions : $\frac{\pi}{12}, \frac{\pi}{4}, \frac{5\pi}{12}$

computed according to (1..6). This 2 times redundant wavelet transform can resolve 6 directions : $\frac{\pi}{12}, \frac{\pi}{4}, \frac{5\pi}{12}$ (see Figure 4). Kingsbury described in [5] a similar construction using complex wavelets. Kingsbury's solution is 4 times redundant. Another construction, that does not result in orthogonal or even biorthogonal wavelets, was obtained using overcomplete steerable filters [4]. Other directionally oriented filter banks were constructed in [2]. While these redundant wavelet transforms can be useful for image analysis, they suffer from the drawback of increasing the number of data by a factor 2 or 4. This becomes a major hurdle to any attempt at computing a sparse representation of an image.

In this work we propose to construct steerable wavelet packets. Inspired by the duality between local trigonometric bases and wavelet packets for a function of one variable [12], we propose to construct wavelet packets of two variables in the Fourier domain using trigonometric bases. We replace the local cosine bases by local Fourier bases. As a result our wavelet packets are complex valued functions with a phase. The construction is performed in the Fourier domain : the Fourier transform of the image is expanded into adjacent local Fourier bases. The method results in an expansion of the image into a set of steerable wavelet packets that we call *brushlets*.

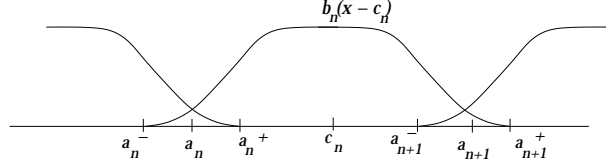


Figure 5. The bell $b_n(x - c_n)$ lives over the interval $[a_n^-, a_{n+1}^+]$.

A key ingredient of the construction of the brushlets is the window used for the local Fourier analysis. Indeed, the Fourier transform of the window constitutes the envelope of a brushlet. We therefore need to use windows that have a very fast decay in the Fourier domain, in order for the envelope to be well localized in space. We will present several choices of windows and study their properties. Finally, we can adaptively select the sizes and locations of the brushlets in order to obtain the most concise and precise representation of an image in terms of oriented textures with all possible directions, frequencies, and locations.

This paper is organized as follows. In the next section we review the construction of orthonormal windowed Fourier bases. This is followed in section 3 by a description of several optimized bells. The biorthogonal brushlet basis is described in section 4.

2. Biorthogonal windowed Fourier bases

As was explained in [12], wavelet packets can be constructed by expanding the Fourier transform of a signal into local cosine bases. We follow this approach and construct two dimensional wavelet packets in the Fourier domain. We replace the cosine bases with Fourier bases that will generate a unique two dimensional frequency. Our decomposition will correspond to a multiscale analysis in the spatial domain. The key ingredient of our construction is a bell used for the local Fourier bases. The design of a bell in the frequency domain is equivalent to the design of wavelet filters.

We review here the construction of smooth biorthogonal windowed Fourier bases in the one dimensional (1-D) case (references on the topic include for instance [1, 3, 16]). In two dimensions (2-D) we use tensor products of 1-D bases. We consider the more general setting where we have two biorthogonal bases [3, 8, 11]. Let $\bigcup_{n=-\infty}^{+\infty} [a_n, a_{n+1}[$ be a cover of \mathbb{R} . We define a neighborhood around each point a_n : $[a_n^-, a_n^+]$, where a_n^-, a_n, a_n^+ are such that (see Figure 5)

$$a_n^- = a_n - \delta < a_n < a_n^+ = a_n + \delta \quad (2..1)$$

Let $l_n = a_{n+1} - a_n$ be the length of the interval $[a_n, a_{n+1}]$, and let $c_n = (a_{n+1} + a_n)/2$ be the center of the interval $[a_n, a_{n+1}]$. Let b_n be a bell function supported

on $[-l_n/2 - \delta, l_n/2 + \delta]$ (see Figure 6) such that

$$\forall x \in [-l_n - \delta, l_n + \delta], \quad b_n^2(x) + b_n^2(2l_n - x) \neq 0 \quad (2..2)$$

and

$$\forall x \in [-l_n + \delta, l_n - \delta], \quad b_n(x) \neq 0 \quad (2..3)$$

We also define the “hump” function h (see Figure 6) :

$$\forall x \in [-\delta, \delta], \quad h(x) = b_n(x - l_n)b_n(x + l_n) \quad (2..4)$$

We only consider the two overlapping case : the bell $b_n(x - c_N)$ only talks to the bells $b_{n-1}(x - c_{n-1})$ and $b_{n+1}(x - c_{n+1})$ (see Figure 5). Let

$$\theta_n(x) = \frac{1}{b_n^2(x) + b_n^2(-2l_n - x) + b_n^2(2l_n - x)} \quad (2..5)$$

then the dual bell \tilde{b}_n is defined as follows:

$$\tilde{b}_n(x) = \begin{cases} \theta_n(x) b_n(x) & \text{if } -l_n - \delta \leq x \leq -l_n + \delta \\ \frac{1}{b_n(x)} & \text{if } -l_n + \delta \leq x \leq l_n - \delta \\ \theta_n(x) b_n(x) & \text{if } l_n - \delta \leq x \leq l_n + \delta \\ 0 & \text{otherwise} \end{cases} \quad (2..6)$$

Let $E_{n,k}(x)$ be the family of complex exponentials on the interval $[a_n, a_{n+1})$:

$$E_{n,k}(x) = \frac{1}{\sqrt{l_n}} e^{-2i\pi k \left(\frac{x - a_n}{l_n} \right)}. \quad (2..7)$$

We define the local Fourier basis functions as

$$u_{n,k}(x) = b_n(x - c_n)E_{n,k}(x) + h(x - a_n)E_{n,k}(2a_n - x) - h(x - a_{n+1})E_{n,k}(2a_{n+1} - x) \quad (2..8)$$

and the dual basis functions are defined as

$$\tilde{u}_{n,k}(x) = \tilde{b}_n(x - c_n)E_{n,k}(x) + \tilde{h}(x - a_n)E_{n,k}(2a_n - x) - \tilde{h}(x - a_{n+1})E_{n,k}(2a_{n+1} - x) \quad (2..9)$$

One can use either one of the two bases to perform the analysis, and compute the coefficients, of a function f . One can then use the other basis for the synthesis, or reconstruction, of the function.

Lemma 1. $u_{n,k}$ and $\tilde{u}_{n,k}$ are Riesz biorthogonal bases:

$$\int u_{n,k}(x) \tilde{u}_{m,j}(x) dx = \delta_{j,k} \delta_{n,m} \quad (2..10)$$

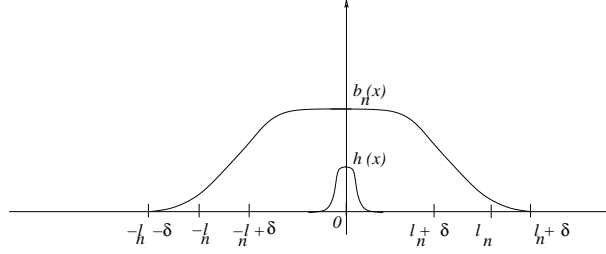


Figure 6. The bell b_n and the hump function h .

$\forall f \in L^2(\mathbb{R})$,

$$\begin{aligned} f(x) &= \sum_{n,k} \tilde{f}_{n,k} u_{n,k}(x) & \tilde{f}_{n,k} &= \int f(x) \tilde{u}_{n,k}(x) dx \\ f(x) &= \sum_{n,k} f_{n,k} \tilde{u}_{n,k}(x) & f_{n,k} &= \int f(x) u_{n,k}(x) dx \end{aligned} \quad (2..11)$$

Furthermore : $\exists B > A > 0$ such that,

$$A \sum_{n,k} |f_{n,k}|^2 \leq \left\| \sum_{n,k} f_{n,k} u_{n,k} \right\|^2 \leq B \sum_{n,k} |f_{n,k}|^2 \quad (2..12)$$

The constants A and B are called the Riesz bounds. If $u_{n,k}$ is an orthonormal sequence, then $A = B = 1$. If f has unit norm, then

$$\frac{1}{B} \leq \sum_{n,k} |f_{n,k}|^2 \leq \frac{1}{A} \quad (2..13)$$

If A is much smaller than 1, then the coefficients $f_{n,k}$ in (2..13) can be very large. Conversely, if B is very large, the coefficients $f_{n,k}$ can become extremely small. In order to obtain decompositions that are numerically stable, and coefficients that neither explode nor vanish, one would like to have Riesz bounds close to 1.

2.1. Implementation by folding

In practice, in order to expand a function f into the basis $u_{n,k}$ we do not calculate the correlation between f and the basis $\{u_{n,k}\}$. Instead we transform f restricted to $[a_n - \delta, a_{n+1} + \delta]$ into a smooth periodic function onto $[a_n, a_{n+1}]$, and expand it into the basis $\{E_{n,k}\}$. To do this we fold the overlapping parts of the window b_n and of the hump function h back into the interval, across the endpoints of the interval, with some folding and unfolding operators. The advantage of the procedure is that we can preprocess the data with the folding operators and then use a conventional FFT to calculate the expansion into the

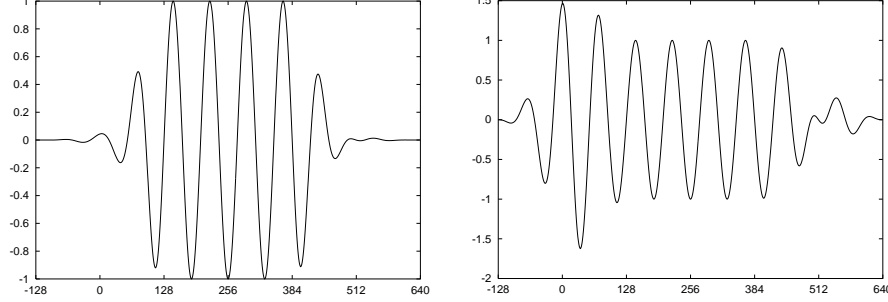


Figure 7. Left : real part of $u_{n,k}$, with $a_n = 0$, $a_{n+1} = 512$, and $\delta = 128$. Right : real part of the dual basis $\tilde{u}_{n,k}$.

basis $\{E_{n,k}\}$. We will follow the construction of Wickerhauser in [1].

Unitary folding and unfolding. We define the unitary folding operator U_{a_n} and its adjoint the unfolding operator $U_{a_n}^*$ as follows:

$$U_{a_n} f(t) = \begin{cases} r\left(\frac{a_n-t}{\delta}\right)f(t) - r\left(\frac{t-a_n}{\delta}\right)f(2a_n-t), & \text{if } a_n - \delta < t < a_n, \\ r\left(\frac{t-a_n}{\delta}\right)f(t) + r\left(\frac{a_n-t}{\delta}\right)f(2a_n-t), & \text{if } a_n < t < a_n + \delta, \\ f(t), & \text{otherwise;} \end{cases} \quad (2.1.1)$$

$$U_{a_n}^* f(t) = \begin{cases} r\left(\frac{a_n-t}{\delta}\right)f(t) + r\left(\frac{t-a_n}{\delta}\right)f(2a_n-t), & \text{if } a_n - \delta < t < a_n, \\ r\left(\frac{t-a_n}{\delta}\right)f(t) - r\left(\frac{a_n-t}{\delta}\right)f(2a_n-t), & \text{if } a_n < t < a_n + \delta, \\ f(t), & \text{otherwise.} \end{cases} \quad (2.1.2)$$

We can then define the periodized folding and unfolding operators. These operators fold and unfold the right end of the segment with the left end. The periodized folding operator $W_{a_n, a_{n+1}}$ and its adjoint $W_{a_n, a_{n+1}}^*$ are defined as follows:

$$W_{a_n, a_{n+1}} f(t) = \begin{cases} r\left(\frac{t-a_n}{\delta}\right)f(t) + r\left(\frac{a_n-t}{\delta}\right)f(a_n + a_{n+1} - t), & \text{if } a_n < t < a_n + \delta, \\ r\left(\frac{a_{n+1}-t}{\delta}\right)f(t) - r\left(\frac{t-a_{n+1}}{\delta}\right)f(a_n + a_{n+1} - t), & \text{if } a_{n+1} - \delta < t < a_{n+1}, \\ f(t), & \text{otherwise;} \end{cases} \quad (2.1.3)$$

$$W_{a_n, a_{n+1}}^* f(t) = \begin{cases} r\left(\frac{t-a_n}{\delta}\right)f(t) - r\left(\frac{a_n-t}{\delta}\right)f(a_n + a_{n+1} - t), & \text{if } a_n < t < a_n + \delta, \\ r\left(\frac{a_{n+1}-t}{\delta}\right)f(t) + r\left(\frac{t-a_{n+1}}{\delta}\right)f(a_n + a_{n+1} - t), & \text{if } a_{n+1} - \delta < t < a_{n+1}, \\ f(t), & \text{otherwise;} \end{cases} \quad (2.1.4)$$

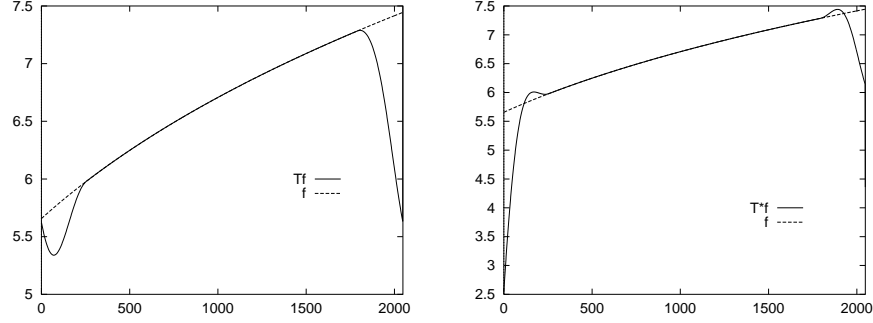


Figure 8. Left : result of the smooth periodic restriction operator. Right : result of the adjoint of the smooth periodic restriction operator .

Let $\mathbb{I}_{a_n, a_{n+1}}$ be the restriction operator:

$$\mathbb{I}_{a_n, a_{n+1}} f = \begin{cases} f(x), & \text{if } x \in [a_n, a_{n+1}] \\ 0, & \text{otherwise} \end{cases} \quad (2.1.5)$$

We can then use folding and unfolding to build an orthogonal transformation that restricts the function to an interval, and periodizes the function while preserving smoothness. We define the *smooth periodic restriction operator* $T_{a_n, a_{n+1}}$ as follows

$$T_{a_n, a_{n+1}} f = W_{a_n, a_{n+1}}^* \mathbb{I}_{a_n, a_{n+1}} U_{a_n} U_{a_{n+1}} f \quad (2.1.6)$$

Let $T_{a_n, a_{n+1}}^*$ be the adjoint of $T_{a_n, a_{n+1}}$

$$T_{a_n, a_{n+1}}^* f = U_{a_n}^* U_{a_{n+1}}^* \mathbb{I}_{a_n, a_{n+1}} W_{a_n, a_{n+1}} f \quad (2.1.7)$$

A simple calculation shows that applying the operator $T_{a_n, a_{n+1}}^*$ to the basis $E_{n,k}$ gives us the basis $u_{n,k}$

$$u_{n,k} = T_{a_n, a_{n+1}}^* E_{n,k} \quad (2.1.8)$$

and we have

$$T_{a_n, a_{n+1}}^* T_{a_n, a_{n+1}} = U_{a_n}^* U_{a_{n+1}}^* \mathbb{I}_{a_n, a_{n+1}} U_{a_n} U_{a_{n+1}} \quad (2.1.9)$$

Figure 8 shows the result of the periodized folding and unfolding operators. The coefficients $f_{n,k} = \langle f, u_{n,k} \rangle$ can then be calculated by expanding $T_{a_n, a_{n+1}} f$ into the basis $E_{n,k}$

$$\langle f, u_{n,k} \rangle = \langle f, T_{a_n, a_{n+1}}^* E_{n,k} \rangle = \langle T_{a_n, a_{n+1}} f, E_{n,k} \rangle \quad (2.1.10)$$

To summarize, the inner product $\langle f, u_{n,k} \rangle$ is calculated as follows:

1. calculate $T_{a_n, a_{n+1}} f$ using the folding operator $T_{a_n, a_{n+1}}$,

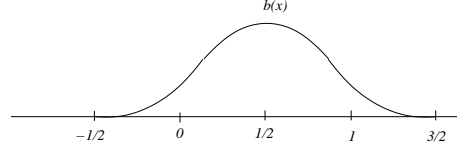


Figure 9. The bell b lives over the interval $[-1/2, 3/2]$.

2. expand $T_{a_n, a_{n+1}} f$ into $E_{n,k}$ using an FFT.

Conversely the reconstruction of f from $\langle f, u_{n,k} \rangle$ is done as follows

1. recover $T_{a_n, a_{n+1}} f$ using an inverse FFT,
2. calculate the smooth orthogonal projection $P_{a_n, a_{n+1}} f = T_{a_n, a_{n+1}}^* T_{a_n, a_{n+1}} f$ using the folding operator $T_{a_n, a_{n+1}}^*$,
3. add successive $P_{a_n, a_{n+1}} f$ to recover the complete signal $f = \sum_{n \in \mathbb{Z}} P_{a_n, a_{n+1}} f$.

3. Choice of the bell function

The key to the success of the brushlet is a bell function b_n that satisfies the conditions (2.2) and (2.3), and that has a Fourier transform with a fast decay. In this section we describe several “optimized” bells that were constructed recently [7, 8]. All bells b_n are obtained from a prototype bell b by translation by $(l_n + \delta)/2$, and by dilation by $l_n + \delta$:

$$b_n(x) = b\left(\frac{x}{l_n + \delta} + \frac{1}{2}\right). \quad (3.1)$$

The prototype bell b is defined on $[-1/2, 3/2]$ (see Figure 9).

3.1. The orthonormal bell of Wickerhauser

The simplest orthonormal bell b is given by :

$$b(x) = \sin \frac{\pi}{2}(x + 1/2). \quad (3.1.1)$$

Unfortunately, this bell is not differentiable at $x = -1/2$ and $3/2$, and therefore will have a very slow decay in the frequency domain. Wickerhauser made $b(x)$ in (3.1.1) smoother by “flattening” it at both end points. For $x \in [-1/2, 1/2]$, and $s \in \mathbb{N}$, he defines

$$b^s(x) = \sin \frac{\pi}{2}(x_s + 1/2) \quad (3.1.2)$$

with

$$x_0 = x \quad \text{and} \quad x_j = \frac{1}{2} \sin(\pi x_{j-1}). \quad (3.1.3)$$

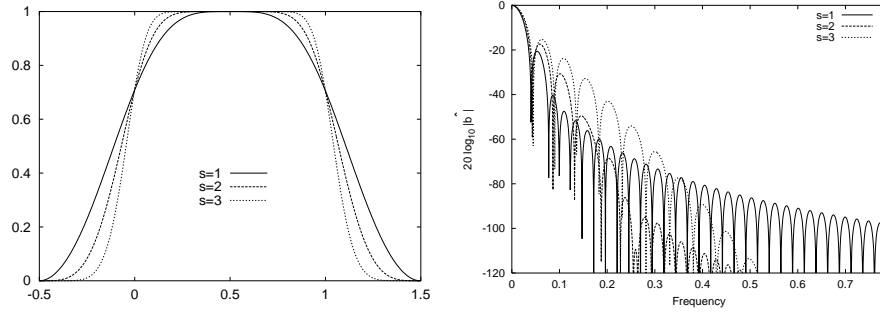


Figure 10. Left : orthonormal bells b^s , $s = 1, 2, 3$. Right : magnitude of the Fourier transform of b^s .

This bell is symmetric : if $x \in [1/2, 3/2]$ we define $b^s(x) = b^s(1 - x)$ (see Figure 10). One can show by induction that b^s has $2^s - 1$ vanishing derivatives at $-1/2$ and $3/2$, and thus $b^s \in C^{2^s-1}$. This bell gives rise to an orthonormal basis. The magnitude of the Fourier transform of b^s (for an interval of $N=512$ samples) is shown in Figure 10. As s increases the main lobe becomes slightly wider, but the side lobes become much smaller.

3.2. Optimized bell of Matviyenko

Matviyenko constructed some optimized bells [8]. He considered the approximation of the constant $p^0 \equiv 1$ over the interval $[a_n, a_{n+1})$ generated from the first K coefficients $p_{n,k}^0, k = 0, \dots, K-1$:

$$\sum_{k=0}^{K-1} p_{n,k}^0 \tilde{\psi}_{n,k} \quad \text{with} \quad p_{n,k}^0 = \int p^0(x) \psi_{n,k}(x) dx \quad (3.2.1)$$

The norm of the residual error is

$$\left\| \sum_{k=K}^{\infty} p_{n,k}^0 \tilde{\psi}_{n,k} \right\|_2^2 \quad (3.2.2)$$

Matviyenko argues in [8] that this family of bells should yield a sparse representation of oscillatory signals of the form $c(x) = \cos(\omega x + \varphi)$.

Instead of reproducing exactly p^0 with one coefficient, Matviyenko designed a family of bells that minimize the residual error (3.2.2). Matviyenko shows that minimizing the sum

$$\sum_{k=K}^{\infty} |p_{n,k}^0|^2 \quad (3.2.3)$$

is related to minimizing the residual error (3.2.2). He then finds the bell b that

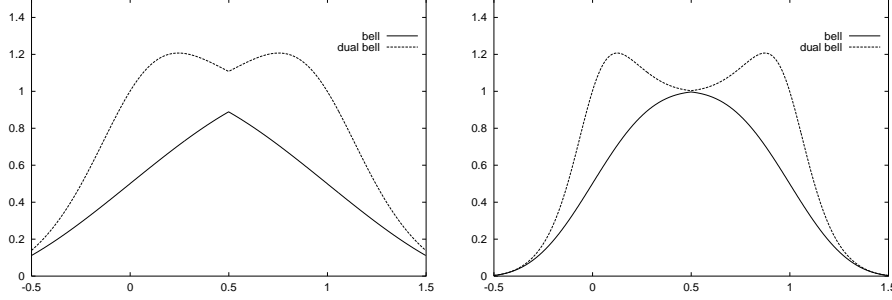


Figure 11. Matviyenko's optimized bell b^K , and dual bell \tilde{b}^K , for $K = 1$ (left), $K = 3$ (right) .

minimizes (3.2.3) under the constraint :

$$b(x) + b(-x) = 1 \quad \text{for all } x \in [0, 1/2]. \quad (3.2.4)$$

The solution of the optimization problem is a bell $b^K(x)$ given by :

$$b^K(x) = \begin{cases} \frac{1}{2}(1 + \sum_{k=0}^{K-1} g_k \sin(k + 1/2)\pi x) & \text{if } -0.5 \leq x \leq 0.5 \\ \frac{1}{2}(1 + \sum_{k=0}^{K-1} (-1)^k g_k \cos(k + 1/2)\pi x) & \text{if } 0.5 \leq x \leq 1.5 \\ 0 & \text{otherwise} \end{cases} \quad (3.2.5)$$

The g_k are calculated numerically in [8]. K influences the steepness of the bell. All bells b_K are bounded by 1, and the dual bells \tilde{b}_K are bounded by $(\sqrt{2}+1)/2$. These bounds guarantee that the Riesz bounds will be $A = 1$ and $B = 2$ for all K . Figure 11 shows the bell b^K and the dual bell \tilde{b}^K for $K = 1$ and 3. The magnitude of the Fourier transform of the bells b^K and \tilde{b}^K (for an interval of $N=512$ samples) is shown in Figure 12. As K increases the side lobes become much smaller. This observation, and equation (3.2.3) seems to indicate that a large K should provide a smaller error, and a better frequency resolution. In practice, as shown in [9], small values of K often provide better performances. One can either choose to use b^K or \tilde{b}^K to compute the coefficients. Because b^K is optimized to minimize the residual error, one should use b^K for the analysis and \tilde{b}^K for the reconstruction.

3.3. Modulated Lapped Biorthogonal Transform (MLBT)

A simple way to smooth $\sin \frac{\pi}{2}(x + 1/2)$ at both end-points is to take the square of the bell. As a result the following bell is in $C^1(\mathbb{R})$:

$$b(x) = \begin{cases} \sin^2 \left[\frac{\pi}{2}(x + 1/2) \right] = \frac{1 - \cos \pi(x + 1/2)}{2} & \text{if } x \in [-1/2, 1/2] \\ b(x) = b(1 - x) & \text{if } x \in [1/2, 3/2] \end{cases} \quad (3.3.1)$$

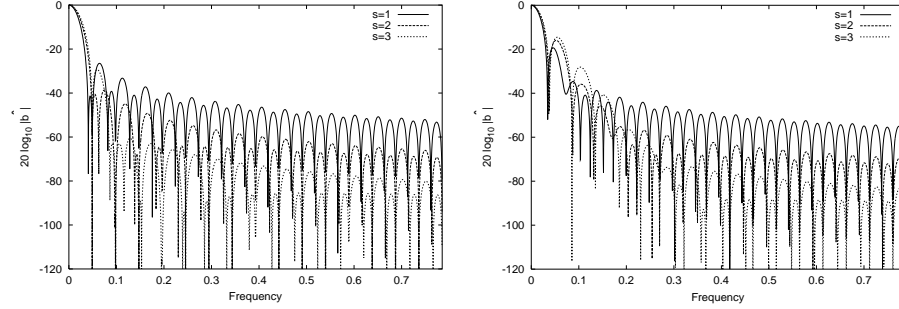


Figure 12. Left : Matviyenko's bell : magnitude of the Fourier transform of b^K . Right : magnitude of the Fourier transform of \tilde{b}^K .

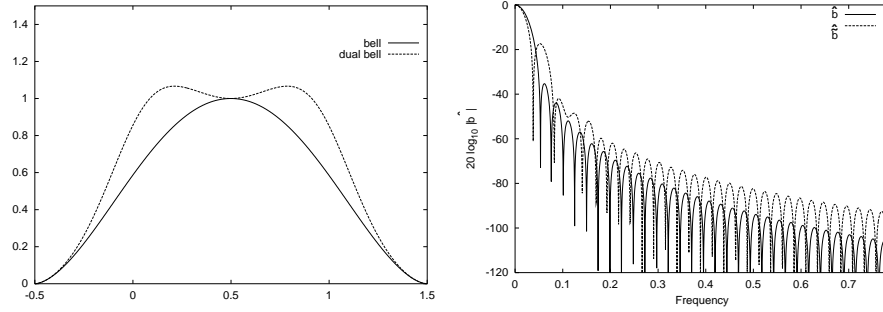


Figure 13. MLBT's bell b and the associated dual bell \tilde{b} . Right : magnitude of the Fourier transform of b and \tilde{b} .

Malvar proposed in [7] the following dual bell :

$$\tilde{b}(x) = \begin{cases} \frac{1 - \cos[\pi(x + 1/2)^\alpha] + \beta}{2 + \beta} & \text{if } x \in [-1/2, 1/2] \\ b(x) = b(1 - x) & \text{if } x \in [1/2, 3/2] \end{cases} \quad (3.3.2)$$

For $\alpha = 1$ and $\beta = 0$ we clearly find the square of $\sin \frac{\pi}{2}(x + 1/2)$. The bell is $C^1(\mathbb{R})$ if $\alpha \geq 1$. Because the bell is smoother, it will have a faster decay in the Fourier domain, and a better frequency selectivity of the associated basis functions [7].

The analysis bell b is derived from the dual bell \tilde{b} using (2.6). In this paper we use the following values of the parameters : $\alpha = 0.85$, and $\beta = 0$. Figure 13 shows the graphs of b and \tilde{b} . The two bells are similar to the optimized bells of Matviyenko. The Riesz bounds are $A = 1$ and $B = 1.458$. The magnitude of the Fourier transform of the analysis bell and the dual bell (for an interval of $N=512$ samples) is shown in Figure 13. The Fourier transform of b has a wider main lobe than the Fourier transform of \tilde{b} but a better stop-band attenuation

(smaller side lobes).

4. Biorthogonal brushlet bases

Inspired by the duality between local trigonometric bases and wavelet packets for a function of one variable [12], we propose to construct wavelet packets of two variables in the Fourier domain using trigonometric bases. We replace the local cosine bases by local Fourier bases.

4.1. One dimensional case

Let $f \in L^2(\mathbb{R})$, and let \hat{f} be the Fourier transform of f . We define a cover of the frequency axis :

$$\bigcup_{n=-\infty}^{n=+\infty} [\omega_n - \frac{l_n}{2}, \omega_n + \frac{l_n}{2}]. \quad (4.1.1)$$

ω_n is the center of each interval of size l_n ¹. Let $u_{n,k}$ be the local Fourier basis associated with this cover. We expand \hat{f} into the basis $u_{n,k}$

$$\hat{f} = \sum \hat{f}_{n,k} u_{n,k} \quad (4.1.2)$$

We then take the inverse Fourier transform . Let $\psi_{n,k}$ the inverse Fourier transform of $u_{n,k}$.

$$f = \sum \hat{f}_{n,k} \psi_{n,k} \quad (4.1.3)$$

Since the Fourier transform is a unitary operator, we obtain a new pair of biorthogonal bases by applying the inverse Fourier transform on $u_{n,k}$ and $\tilde{u}_{n,k}$.

Lemma 2. $\{\psi_{m,j}, \tilde{\psi}_{n,k} \mid j, k, m, n \in \mathbb{Z}\}$ are biorthogonal bases for $L^2(\mathbb{R})$. \square

We call $\{\psi_{n,k}\}$ and $\{\tilde{\psi}_{n,k}\}$ the biorthogonal brushlet basis. From (2..8) we have

$$\psi_{n,k}(x) = \frac{1}{\sqrt{l_n}} e^{2i\pi\omega_n x} \left\{ (-1)^k \hat{b}_n(x - \frac{k}{l_n}) - 2i \sin(\pi l_n x) \hat{h}(x + \frac{k}{l_n}) \right\} \quad (4.1.4)$$

We can introduce the “steepness factor” of the window b_n ,

$$\sigma = \frac{\delta}{l_n} \quad (4.1.5)$$

we also introduce the window b_σ supported on $[-1/2 - \sigma, 1/2 + \sigma]$ such that

$$b_n(x) = b_\sigma(\frac{x}{l_n}) \quad (4.1.6)$$

¹the center of the interval was called c_n when the analysis was performed in the original time domain, since we work in the frequency domain we prefer to use ω_n

and the hump function h_σ supported on $[-\sigma, \sigma]$ such that

$$h(x) = h_\sigma\left(\frac{x}{l_n}\right) \quad (4.1.7)$$

We have

$$\hat{b}_n(x) = l_n \hat{b}_\sigma(l_n x) \quad (4.1.8)$$

then (4.1.4) can be rewritten as follows

$$\psi_{n,k}(x) = \frac{1}{\sqrt{l_n}} e^{2i\pi\omega_n x} \left\{ (-1)^k l_n \hat{b}_\sigma(l_n x - k) - 2i \sin(\pi l_n x) l_n \hat{h}_\sigma(l_n x + k) \right\} \quad (4.1.9)$$

then we have

$$\psi_{n,k}(x) = \sqrt{l_n} e^{2i\pi a_n x} e^{i\pi l_n x} \left\{ (-1)^k \hat{b}_\sigma(l_n x - k) - 2i \sin(\pi l_n x) \hat{h}_\sigma(l_n x + k) \right\} \quad (4.1.10)$$

We note in (4.1.10) that l_n appears as a scaling factor of the analysis, and k is the translation index of the brushlet. $\psi_{n,k}$ has an expression similar to a wavelet, however as opposed to a real valued wavelet, $\psi_{n,k}$ is a complex valued function with a phase. The phase encodes the orientation of the brushlet pattern in the two-dimensional case. b_σ and h_σ are even real valued functions, thus \hat{b}_σ and \hat{h}_σ are also even real valued functions.

The function $\psi_{n,k}$ is composed of two terms, localized around k/l_n , and around $-k/l_n$, that are oscillating with the frequency ω_n . The main term is an exponential multiplied by \hat{b}_σ . Because b_σ is compactly supported, \hat{b}_σ has an infinite support. As explained in the previous section, a careful choice of b allows us to have a Fourier transform \hat{b}_σ with a fast decay.

The envelope of the second term is the Fourier transform of the hump function h . If one chooses \hat{b}_σ with a fast decay, then \hat{h}_σ will also have a fast decay. We can also control the magnitude of \hat{b}_σ using σ : since $|\hat{h}_\sigma(x)| \leq \sigma$, the second term can be made as small as possible. However, when σ tends to zero the first term is not localized anymore. There is a tradeoff between the localization of \hat{b}_σ and the magnitude of the second term.

4.2. Discrete implementation of the brushlet expansion

We assume that the original signal f has been sampled at N equally spaced mesh nodes

$$F_n = f(n\Delta x) \quad n = 0, 1, \dots, N-1 \quad (4.2.1)$$

We calculate the discrete Fourier transform of the sequence F_n using an FFT. We obtain N samples

$$\hat{F}_k = \hat{f}\left(\frac{k}{\Delta x}\right) \quad , \quad k = -\frac{N}{2}, -\frac{N}{2} + 1, \dots, 0, \dots, \frac{N}{2} - 1 \quad (4.2.2)$$

We then divide the set of integers

$$\left\{ -\frac{N}{2}, \dots, \frac{N}{2} - 1 \right\} \quad (4.2.3)$$

into $\frac{N}{l}$ intervals of equal size l . For each interval

$$\left[k \frac{1}{\Delta x}, (k + l - 1) \frac{1}{\Delta x} \right]$$

we expand \hat{F} into the discrete orthonormal windowed Fourier basis. First we calculate $T_{k,k+l-1}(\hat{F})$ using the discrete smooth periodic restriction operator. We then expand $T_{k,k+l-1}(\hat{F})$ into the basis $E_{n,k}$ using an FFT of size l . On $[k \frac{1}{\Delta x}, (k + l - 1) \frac{1}{\Delta x}]$, \hat{F} , is uniquely characterized by the samples at the mesh points

$$\frac{k}{\Delta x}, \dots, \frac{k + l - 1}{\Delta x}$$

Since $T_{k,k+l-1}$ is a unitary isomorphism $T_{k,k+l-1}(\hat{F})$ is also uniquely characterized by the samples

$$\frac{k}{\Delta x}, \dots, \frac{k + l - 1}{\Delta x}$$

Finally the discrete Fourier transform of $T_{k,k+l-1}(\hat{F})$ is characterized by the samples at the mesh points

$$0, \frac{1}{l}\Delta x, \dots, \frac{l-1}{l}\Delta x$$

Let $\Psi_{n,k}$ be the discrete version of the basis function $\psi_{n,k}$. We note that even though the support of $\Psi_{n,k}$ is larger than $[0, \Delta x \frac{l-1}{l}]$, $\Psi_{n,k}$ is entirely characterized by the samples

$$0, \frac{1}{l}\Delta x, \dots, \frac{l-1}{l}\Delta x$$

This result is similar to the subsampling operation in multiresolution analysis [6, 12]. Here the subsampling is performed by selecting subinterval of the global Fourier transform and expanding them into a local Fourier basis. In (4.1.10) we can replace x by the sample $k \frac{\Delta x}{l}$, $k = 0, \dots, l-1$, and l_n by $\frac{l}{\Delta x}$ and we obtain the discrete version of $\psi_{n,k}$:

$$\Psi_{n,k}(k) = \sqrt{l} e^{2i\pi \frac{jk}{l}} e^{i\pi k} \left\{ (-1)^n \hat{b}_\sigma(k-n) - 2i \sin(\pi k) \hat{h}_\sigma(k+n) \right\} \quad (4.2.4)$$

with

$$0 \leq n \leq l-1 \quad \text{and} \quad k = 0, \dots, l-1.$$

Figures 14 and 15 show the basis functions $\Psi_{n,k}$ and the dual function $\tilde{\Psi}_{n,k}$ for

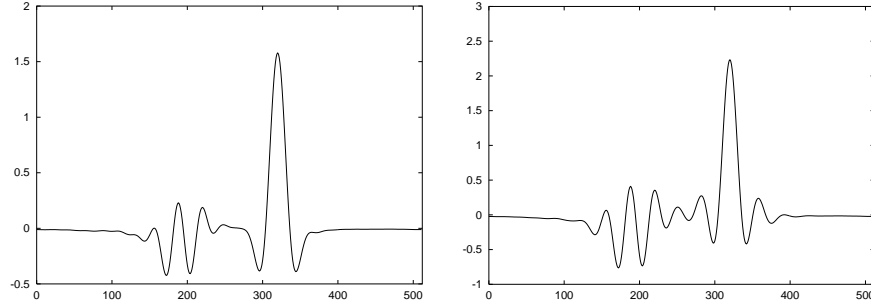


Figure 14. Left : the basis function $\Psi_{n,k}$. Right : the dual function $\tilde{\Psi}_{n,k}$. We used the MLBT window with $\alpha = 0.85$. $N = 512, l = 16, \delta = 8, \omega_n = 8$ and $k = 320$.

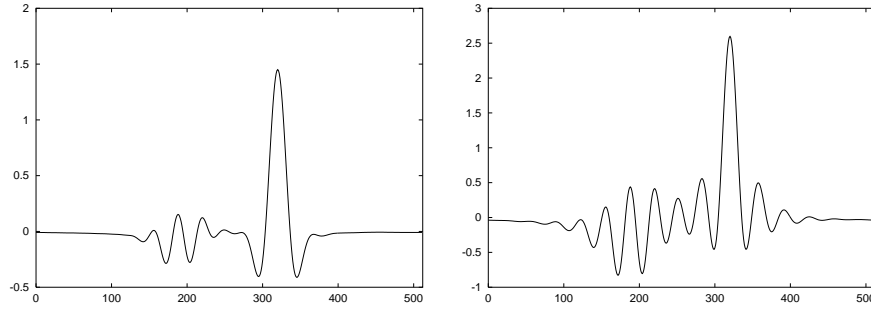


Figure 15. Left : the basis function $\Psi_{n,k}$. Right : the dual function $\tilde{\Psi}_{n,k}$. We used Matviyenko's window with $K = 3$. $N = 512, l = 16, \delta = 8, \omega_n = 8$ and $k = 320$.

two different windows. All the graphs were obtained with $N = 512, l = 16, \delta = 8, \omega_n = 8$ and $k = 320$. In figure 14 we used the MLBT window with $\alpha = 0.85$. In figure 15 we used Matviyenko's window with $K = 3$. The main part of the function $\Psi_{n,0}$ is similar to the scaling function of a wavelet. This should be the case, since $\Psi_{n,0}$ corresponds to the window that is nearest to 0 in the Fourier domain. As expected we observe the Fourier transform of the hump function, \hat{h} , on the left of main part. We can lower the amplitude of \hat{h} in $\Psi_{n,k}$ by having a window b_n that is steeper, or by decreasing δ . Unfortunately, decreasing δ has the effect of spreading the main part of $\Psi_{n,k}$. As we make the window b_n steeper, the Fourier transform of the dual of the hump function, $\hat{\hat{h}}$, becomes larger.

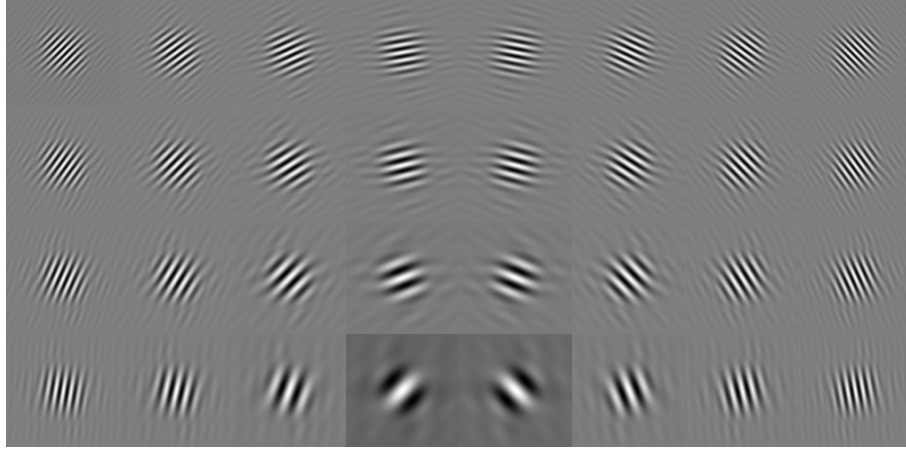


Figure 16. Basis functions $\psi_{m,j} \otimes \psi_{n,k}$ for the frequencies $(m \frac{2\pi}{512}, m \frac{2\pi}{512})$, with $(m, n) \in \{-48, -32, -16, 0, 16, 32, 48\}^2$. $\psi_{n,k}$ is represented as an image, where a large positive value is coded with white, and a large negative value is coded with black. We have $h_m = l_n = 16, \delta = 8$.

4.3. Two-dimensional case

We are now in the position of constructing two dimensional brushlets. We define a partition of the frequency plane obtained by the lattice cubes :

$$\bigcup_{n=-\infty}^{\infty} \bigcup_{m=-\infty}^{\infty} [\xi_m - \frac{h_m}{2}, \xi_m + \frac{h_m}{2}] \otimes [\eta_n - \frac{l_n}{2}, \eta_n + \frac{l_n}{2}] \quad (4.3.1)$$

of the frequency axis. (ξ_m, η_n) is the center of each rectangle of size $h_m \times l_n$. We consider the separable tensor products of bases $\psi_{m,j}$, and $\psi_{n,k}$. We have

Lemma 3. *The sequence $\psi_{m,j} \otimes \psi_{n,k}$ is an orthonormal basis for $L^2(\mathbb{R}^2)$. \square*

We have :

$$\begin{aligned} \psi_{m,j}(x) \otimes \psi_{n,k}(y) = & \sqrt{h_m l_n} e^{2i\pi(\xi_m x + \eta_n y)} \\ & \begin{bmatrix} (-1)^j \hat{b}_\sigma(h_m x - j) - 2i \sin(\pi h_m x) \hat{h}_\sigma(h_m x + j) \\ (-1)^k \hat{b}_\sigma(l_n y - k) - 2i \sin(\pi l_n y) \hat{h}_\sigma(l_n y + k) \end{bmatrix} \end{aligned} \quad (4.3.2)$$

The tensor product $\psi_{m,j}(x) \otimes \psi_{n,k}(y)$ is an oriented pattern oscillating with the frequency (ξ_m, η_n) and localized at $(j/h_m, k/l_n)$. The size of the pattern is inversely proportional to the size of the analyzing window: $h_m \times l_n$ in the Fourier space.

Directional image analysis. Figure 16 shows the basis functions $\psi_{m,j} \otimes \psi_{n,k}$ for several values of the frequency (ξ_m, η_n) , at a fixed scale (i.e fixed h_m and l_n). The function is represented as an image, where a large positive value is coded with white, and a large negative value is coded with black. The image size was 512×512 , and the analysis windows in the Fourier domain were defined by $h_m = l_n = 16, \delta = 8$. The frequencies shown are

$$(m \frac{2\pi}{512}, m \frac{2\pi}{512}) \quad (m, n) \in \{-48, -32, -16, 0, 16, 32, 48\}^2 \quad (4.3.3)$$

This figure illustrates the selective orientation analysis performed by the brushlets : at a given scale the brushlets can resolve many more orientations (10 for this scale) than standard wavelet packets. As the scale get coarser (smaller h_m, l_n), one can resolve even more directions.

Clearly the advantage of the brushlet over a local Fourier analysis stems from the fact that one can perform a multiscale analysis of an image. We illustrate this property with the brushlet expansion of the image Barbara, shown in Figure 17. A first expansion was performed with a tiling of the Fourier plane into four quadrants. We have $x_0 = -256, x_1 = 0, x_2 = 255$, and similarly $y_0 = -256, y_1 = 0, y_2 = 255$. The four sets of brushlets have the orientations $\frac{\pi}{4} + k \frac{\pi}{2}, k = 0, \dots, 3$. Figure 18 shows the imaginary part of the brushlets coefficients for each of the four quadrants of the Fourier plane. Since the signal is real, the coefficients are antisymmetric with respect to the origin. The upper right quadrant contains textures with patterns oriented along the direction $\frac{\pi}{4}$: the right leg, the mouth, the eyes, and the left arm. In the upper left window, textures with patterns oriented along the direction $\frac{3\pi}{4}$: the left leg, the nose, the right arm.

A second expansion has been performed using a finer grid. Each quadrant was further divided into four quadrants. The brushlet expansion was calculated for this finer tiling. The sixteen set of brushlets have twelve different orientations as shown in Figure 19. The orientations $\frac{\pi}{4} + k \frac{\pi}{2}$ are associated with two different frequencies. Figure 19 shows the imaginary part of the brushlet expansion. Again the coefficients are antisymmetric with respect to the origin. The four lattice squares around the origin characterize the DC terms of the expansion. The other squares correspond to higher frequency textures. We note that the texture of the legs, and on the scarf have been completely removed from the four DC regions, and are present in the regions that have the directions 1 and 12 as shown in Figure 19.

We note that the decomposition achieved by wavelet packets does not permit us to localize a unique frequency, for instance in the positive part of the Fourier space. Indeed two symmetric windows are always associated with a real wavelet. As a result a wavelet packet expansion will require many more coefficients to describe a pattern with an arbitrary orientation; whereas the same pattern can be coded with a single brushlet coefficient.

Directionally oriented filter banks (e.g. [2, 15]) have been used for image compression and image analysis. They do not allow however an arbitrary partitioning of the Fourier plane. Furthermore in our method the tiling can be adapted to the image content : we can adaptively select the size and location of the windows $[\xi_m - h_m/2, \xi_m + h_m/2] \otimes [\eta_n - l_n/2, \eta_n + l_n/2]$ with the best basis algorithm.



Figure 17. Original 512 x 512 Barbara image .

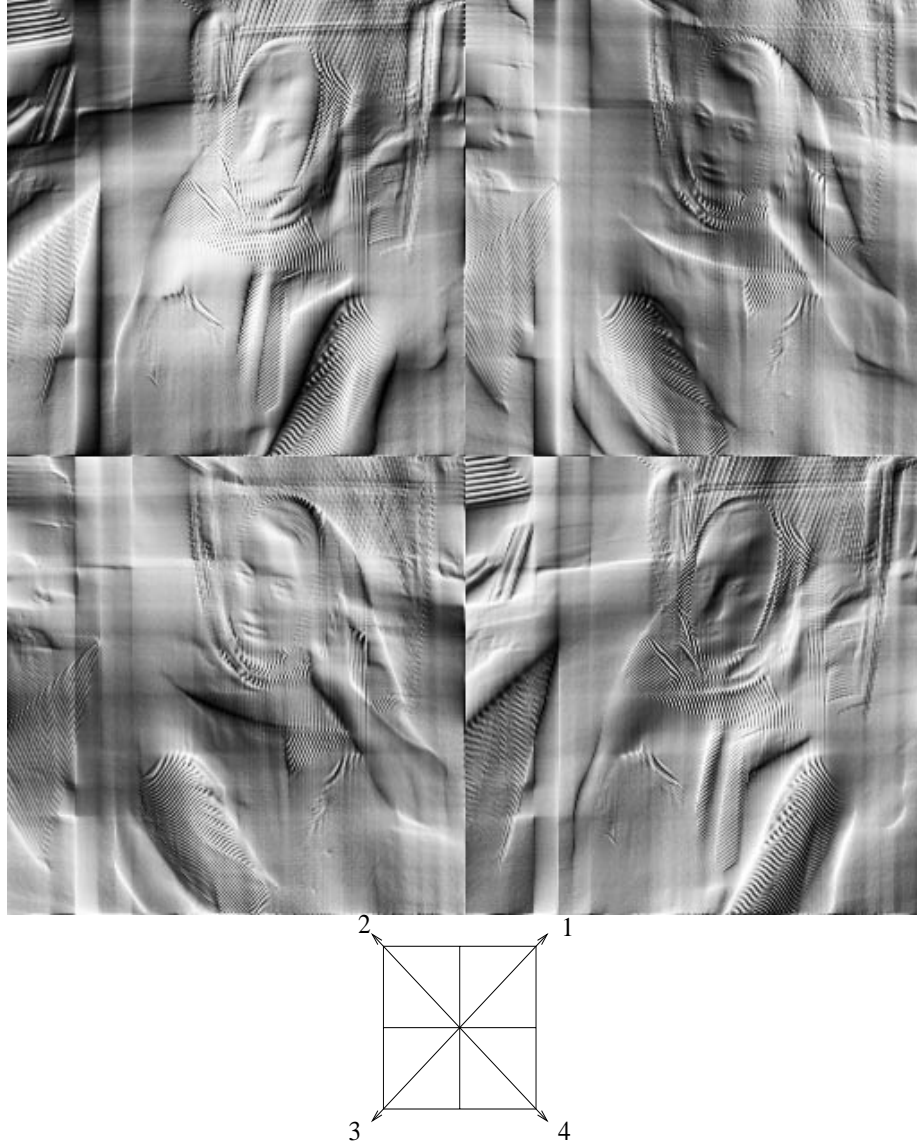


Figure 18. Imaginary part of the brushlets coefficients for each of the four quadrants of the Fourier plane. Since the signal is real, the coefficients are antisymmetric with respect to the origin. The upper right quadrant contains textures with patterns oriented along the direction $\frac{\pi}{4}$: the right leg, the mouth, the eyes, and the left arm. In the upper left window, textures with patterns oriented along the direction $\frac{3\pi}{4}$: the left leg, the nose, the right arm .

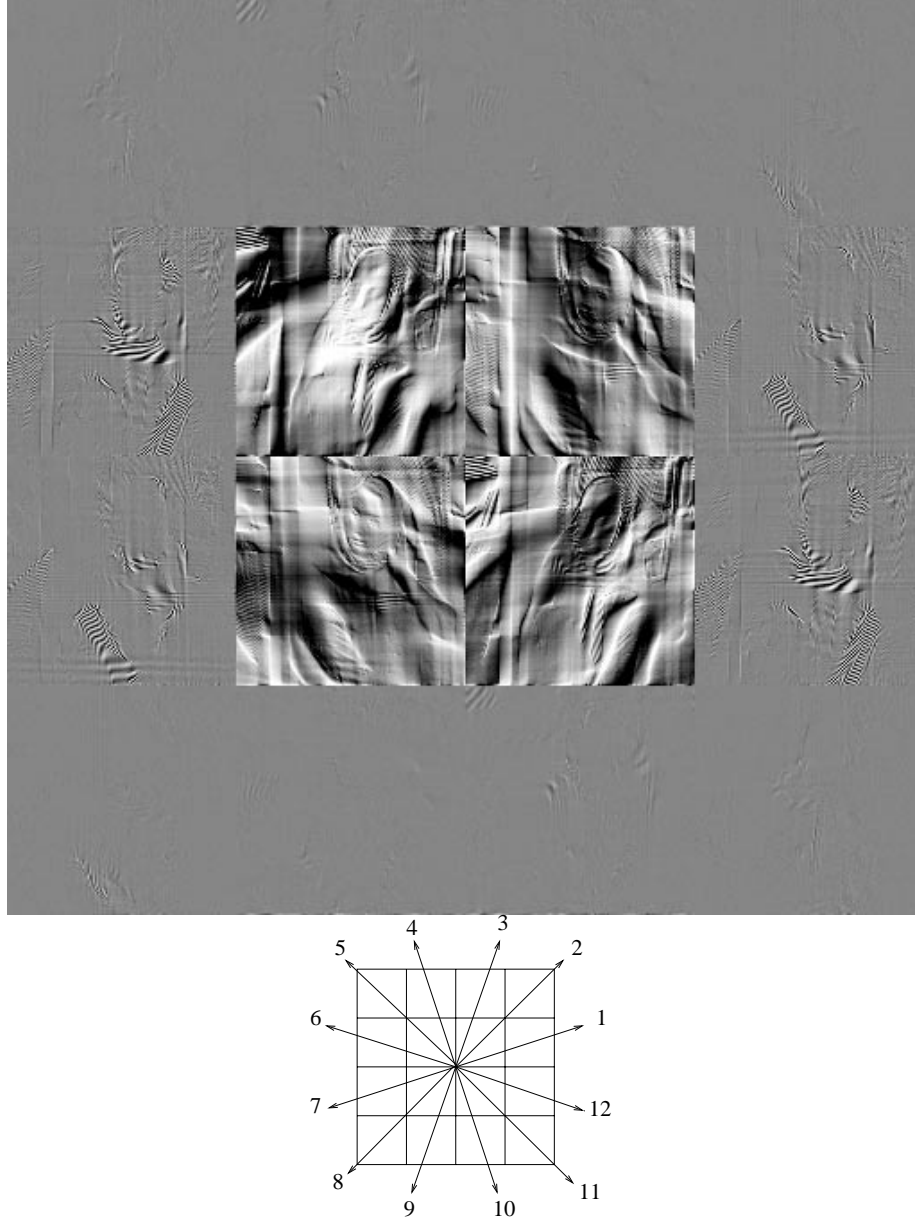


Figure 19. Imaginary part of the brushlet expansion. The four lattice squares around the origin characterize the DC terms of the expansion. The other squares correspond to higher frequency textures. The texture of the legs, and on the scarf have been completely removed from the four DC regions, and are present in the regions that have the directions 1 and 12. .



Figure 20. These simple images cannot be coded efficiently with any existing transform : wavelets, Fourier, DCT, brushlets, etc. .

5. Conclusion

We have addressed the problem of describing an image with a library of steerable wavelet packets. Inspired by the duality between local trigonometric bases and wavelet packets, we constructed wavelet packets of two variables in the Fourier domain using local Fourier bases. Our wavelet packets are complex valued functions with a phase. We have shown that the brushlets can resolve without any ambiguity many more orientations than standard wavelet packets. In theory our brushlets have infinite support. However we have shown that a careful design of the window of the local Fourier basis yields a brushlet with a very fast decay.

This construction demonstrates that there are many other ways to analyze and represent images that go beyond the standard bi-dimensional wavelet transform. We believe that the following questions are areas for future studies, and will give rise to more “natural” basis functions for images.

1. Our brushlets have a square support. One should be able to construct elongated brushlets with several possible aspect ratio. One approach to this problem consists in resampling the Fourier transform \hat{f} in polar coordinates (ρ, θ) and expanding $\hat{f}(\rho, \theta)$ with local Fourier bases.
2. We have only investigated the efficient representation of periodic patterns. Many other type of texture exist in images. The texture formed by the coffee beans or the flowers in the images shown in Figure 20 cannot be efficiently coded by brushlets. In fact, these deceptively simple images cannot be efficiently coded with any transform that is available to us today : wavelet transform, Fourier transform, etc.

References

- [1] P. Auscher, G. Weiss, and M.V. Wickerhauser, *Local sine and cosine bases of Coifman and Meyer*, Wavelets-A Tutorial, Academic Press, 1992, pp. 237–256.
- [2] R.H. Bamberger and M.J.T. Smith, *A filter bank for the directional decomposition of images: theory and design*, IEEE Trans. on Signal Processing (1992), 882–893.
- [3] C.K. Chui and X. Shi, *Characterization of biorthogonal cosine wavelets*, J. Fourier Anal. Appl. **3** (1997), no. 5, 560–575.
- [4] W.T. Freeman and E.H. Adelson, *The design and use of steerable filters*, IEEE Trans. PAMI **13**, No9 (1991), 891–906.
- [5] N. Kingsbury, *Image processing with complex wavelets*, Phil. Trans. R. Soc. Lond. A **357** (1999), 2543–2560.
- [6] S. Mallat, *A wavelet tour of signal processing*, Academic Press, 1999.
- [7] H.S. Malvar, *Biorthogonal and nonuniform lapped transforms for transform coding with reduced blocking and ringing artifacts*, IEEE Transactions on Signal Processing **46**(4) (1998), 1043–1053.
- [8] G. Matviyenko, *Optimized local trigonometric bases*, Applied and Computational Harmonic Analysis **3** (1996), 301–323.
- [9] F.G. Meyer, *Image compression with adaptive local cosines : A comparative study*, International Conference on Image Processing, ICIP'01, Thessaloniki, Greece, Oct. 2001, IEEE Press, 2001.
- [10] F.G. Meyer, A.Z. Averbuch, and J-O. Strömberg, *Fast adaptive wavelet packet image compression*, IEEE Trans. on Image Processing (2000), 792–800.
- [11] F.G. Meyer and R.R. Coifman, *Brushlets: a tool for directional image analysis and image compression*, Applied and Computational Harmonic Analysis (1997), 147–187.
- [12] Y. Meyer, *Wavelets and operators*, Cambridge University Press, 1993.
- [13] K. Ramchandran and M. Vetterli, *Best wavelet packet bases in a rate-distortion sense*, IEEE Trans. on Image Processing **2** (1993), no. 2, 160–175.
- [14] I. Selesnick, *The design of Hilbert transform pairs of wavelet bases, to appear in IEEE Trans. on Signal Processing*, 2001.

- [15] E.P. Simoncelli and E.H. Adelson, *Nonseparable extensions of quadrature mirror filters to multiple dimensions*, Proc. of the IEEE (1990), 652–664.
- [16] M.V. Wickerhauser, *Adapted wavelet analysis from theory to software*, A.K. Peters, 1995.

François G. Meyer
Department of Electrical Engineering
University of Colorado at Boulder
Boulder CO, 80309
francois.meyer@colorado.edu

Ronald R. Coifman
Department of Mathematics
Yale University,
New Haven CT, 06520
coifman@math.yale.edu